JOURNAL OF CATALYSIS 57, 339–360 (1979)

Catalytic Synthesis of Methanol from CO/H_2

II. Electron Microscopy (TEM, STEM, Microdiffraction, and Energy Dispersive Analysis) of the Cu/ZnO and $Cu/ZnO/Cr_2O_3$ Catalysts

S. MEHTA, G. W. SIMMONS, K. KLIER, AND R. G. HERMAN

Center for Surface and Coatings Research, Lehigh University, Bethlehem, Pennsylvania 18015

Received August 16, 1978; revised November 21, 1978

Transmission electron microscopy of the Cu/ZnO and $Cu/ZnO/Cr_2O_3$ methanol synthesis catalysts was used to characterize the dispersions of CuO, ZnO, and Cr_2O_3 in the calcined catalysts and Cu metal, ZnO, and Cr_2O_3 in the reduced and used catalysts. All components were found to have morphologies of their independently existing dispersions except ZnO, which appeared as a network of thin crystallites at Cu concentrations of 30% and less and as well-developed individual hexagonal platelets at higher Cu concentrations. The hexagonal platelet morphology was probably induced by epitaxial growth of ZnO on $Cu_2(OH)_3NO_3$ during calcination. Microdiffraction in the scanning transmission electron microscope and selected area diffraction in the transmission electron microscope showed that the network of ZnO crystallites had the hexagonal crystal axis parallel to their major surface plane and the platelet ZnO particles had the hexagonal crystal axis perpendicular to the platelet plane. Quantitative elemental analyses of the individual particles in the composite catalysts were carried out by characteristic X-ray emission in the energy dispersive mode. It was found that both ZnO morphologies in the reduced Cu/ZnO catalysts contained up to 12% copper and in the $Cu/ZnO/Cr_2O_3$ catalysts up to 16% copper accompanied by Cr(III). These results were interpreted as a dissolution of copper in ZnO in the form of Cu(I) that was assisted by the presence of a trivalent ion. The Cu(I)/ZnO solution, which was earlier found to have characteristic optical absorption in the near infrared, was proposed to be the active component of the low pressure methanol synthesis catalysts.

I. INTRODUCTION

In Part I of this communication (*1*) the variations of catalytic activity with composition were reported for the low pressure (to 100 atm) methanol synthesis catalysts based on copper, zinc oxide, and chromia or alumina. It was established that neither chromia nor alumina were essential for the high catalyst activity and selectivity; however, a *simultaneous* presence of copper and zinc oxide appeared necessary for the low pressure synthesis. These observations suggested that a chemical or physical interaction between the two components, copper and zinc oxide, played an important role in the formation of an active catalyst. Strong interactions in the Cu/ZnO system were indeed indicated by the black color and a characteristic near-infrared absorption that was attributed to a solution of Cu(I) ions in the zinc oxide phase. A synthesis mechanism was proposed in which the Cu(I) centers adsorbed and activated carbon monoxide while the zinc oxide supplied the hydrogenation function.

To provide further insight into the chemical and physical interactions in the mixed catalysts and to specify the condi-

0021-9517/79/060339-22$02.00/0
Copyright © 1979 by Academic Press, Inc.
All rights of reproduction in any form reserved.

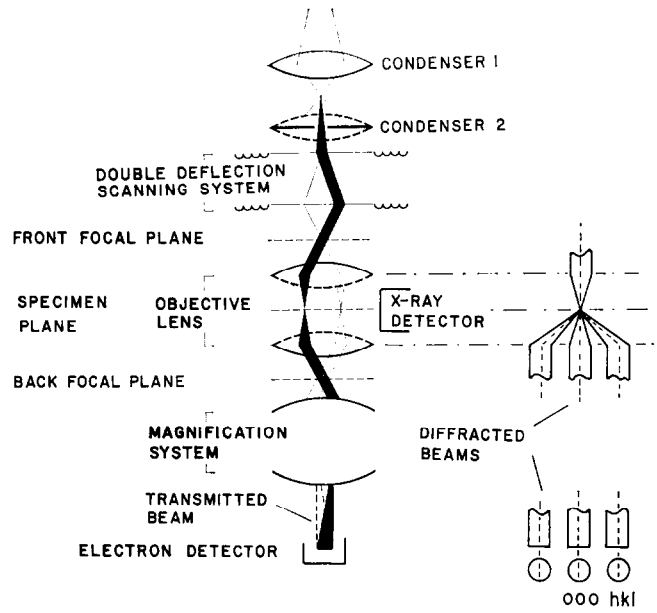

FIG. 1. Schematic diagram showing the operating principles of STEM. Images are obtained by measuring the variation in intensity of the transmitted electron beam as a function of incident beam position. Composition is obtained with an energy dispersive X-ray detector in the specimen plane. The origin of the disks (rather than spots) under convergent beam diffraction conditions is shown on the right side of the diagram.

tions under which active catalysts may be formed, the present study was undertaken to investigate the morphology, crystal structure, and elemental composition, particularly the Cu content in ZnO, of the individual catalyst particles. These properties were studied by scanning electron microscopy (SEM), transmission electron microscopy (TEM), and scanning transmission electron microscopy (STEM). The characteristic morphologies of each catalyst composition were determined in relation to the crystal structures of the individual components of the working catalysts and of their precursors. Simultaneous microdiffraction and characteristic X-ray emission analyses in STEM were used to assay the content of one catalyst component in another and to investigate whether the mutual solubility affected the crystal structure of the individual particles in the mixed catalysts. Results of these structural and elemental analyses were found useful, in conjunction with spectroscopic and surface analytical observations reported elsewhere (*1*, *2*), for the elucidation of the promotion effects in the Cu/ZnO catalysts.

II. EXPERIMENTAL

Materials. For a systematic characterization of the methanol catalysts, the following materials were studied: pure ZnO, CuO, Cu, and Cr_2O_3, binary CuO/ZnO and Cu/ZnO over a range of compositions from 2/98 to 67/33, and ternary $CuO/ZnO/Cr_2O_3$ and $Cu/ZnO/Cr_2O_3$ with a composition 60/30/10. Zinc oxide and copper(II) oxide were prepared by precipitating the basic salts of zinc and copper from nitrate solutions with sodium carbonate and then calcining the respective precipitates by gradually increasing the temperature to 350°C (*1*). Copper was prepared by reduction of the cupric oxide in H_2/N_2 (2%/98%) at 250°C. Specimens

of chromia were obtained from a commercially available, reagent grade source. The binary mixtures were prepared by coprecipitation from nitrate solutions containing specific ratios of copper and zinc. The CuO/ZnO specimens were obtained by calcination of the coprecipitates and Cu/ZnO specimens by the reduction of the oxides. The ternary mixtures were prepared in the same manner as the binary catalysts

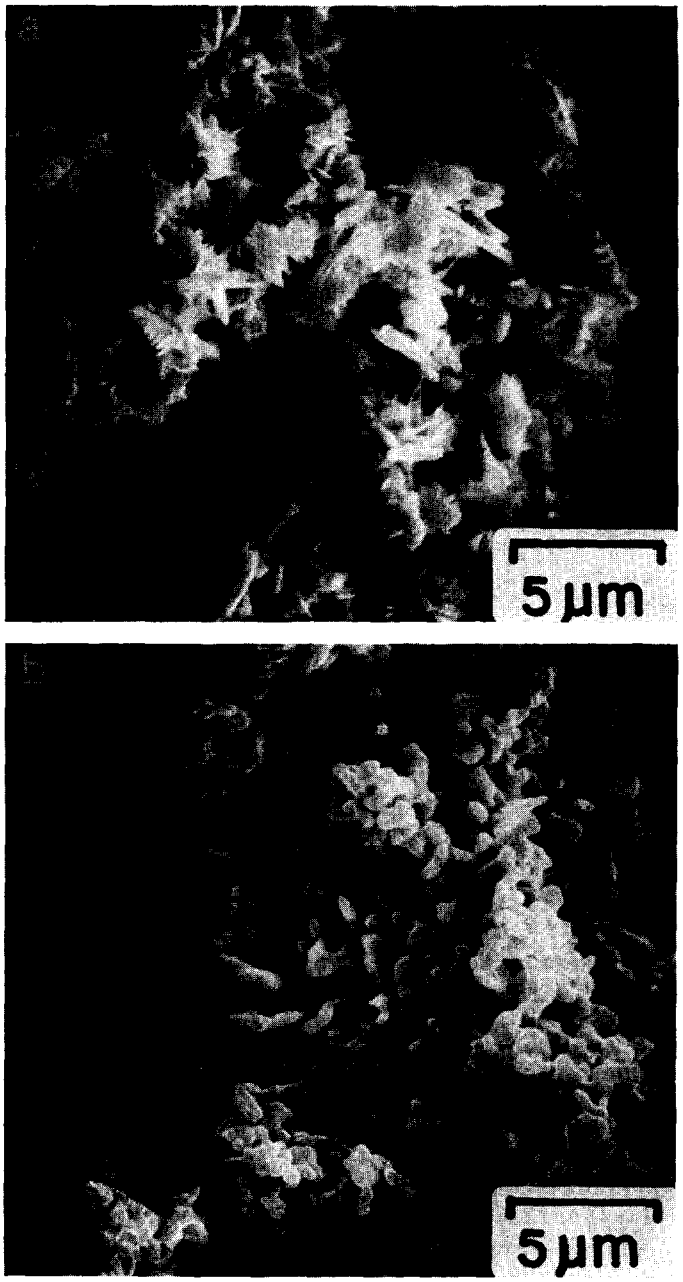

FIG. 2. Scanning electron micrographs of (a) CuO, (b) Cu, and (c) Cr_2O_3.

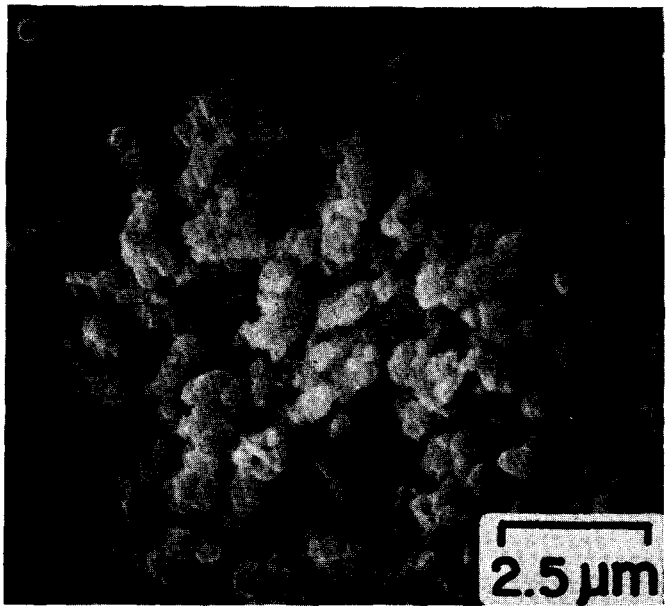

FIG. 2—*Continued.*

with the addition of reagent grade chromia after completion of the precipitation step. Copper, ZnO, Cu/ZnO and Cu/ZnO/Cr_2O_3 were tested for catalytic activity at 75 atm and 200 to 300°C. Test results and further details of the catalyst preparations have been reported in Part I.

Sample preparation. Catalyst specimens suitable for both transmission electron microscopy (TEM) and scanning transmission electron microscopy (STEM) were prepared by ultrasonically dispersing the materials in ethyl alcohol. To obtain specimens that contained particles representative of the catalysts, a standard stainless steel electron microscope grid coated with approximately 40 nm Formvar/carbon support film was passed through the suspension as long as the latter was uniformly dispersed. The grid was allowed to dry in a dust-free environment and then coated with 20 to 40 nm thick carbon film to reduce electrostatic charging of the particles by the incident electron beam. Beryllium grids and a beryllium filtering holder were used in STEM to minimize stray background X rays during the X-ray microanalysis. The Formvar/carbon covered grid containing the specimen was outgassed in vacuum at 180 to 200°C for 20 min to reduce the rate of specimen contamination when long observation times were required with a stationary probe.

For those materials that were examined with conventional scanning microscopy (SEM), the specimens were prepared by placing a drop of the suspension on the surface of an aluminum pedestal, allowing the suspension to dry and then coating the specimen with carbon.

Instrumentation. A Phillips 300 transmission microscope was used for both the TEM and STEM studies. This instrument has been modified to accommodate the electron optics, scanning coils, electron detector, and energy dispersive analyzer so that the microscope could be conveniently converted to the STEM mode of operation. An ETEC Autoscan scanning electron microscope equipped with an energy dispersive detector was used for the SEM studies.

Since transmission electron microscopy, selected area electron diffraction, and dark field electron microscopy are well-established techniques, no detailed description of these methods will be given. Conventional scanning electron microscopy techniques are likewise well known and details can be found elsewhere. The scanning transmission electron microscopy, on the other hand, is a relatively new technique (*3*), and therefore some of its essential features are outlined below. A schematic diagram of the operating principles of STEM are shown in Fig. 1. In STEM, a

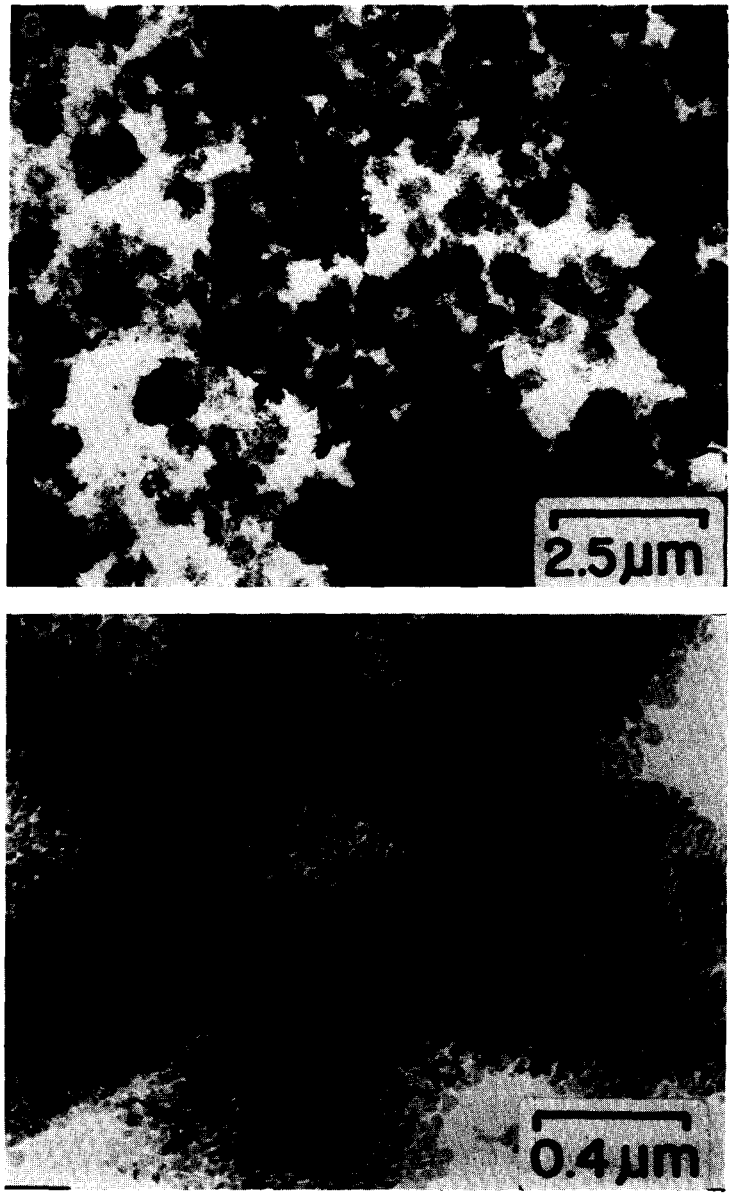

FIG. 3. Transmission electron micrographs of pure zinc oxide prepared by calcination of $Zn_5(OH)_6(CO_3)_2$.

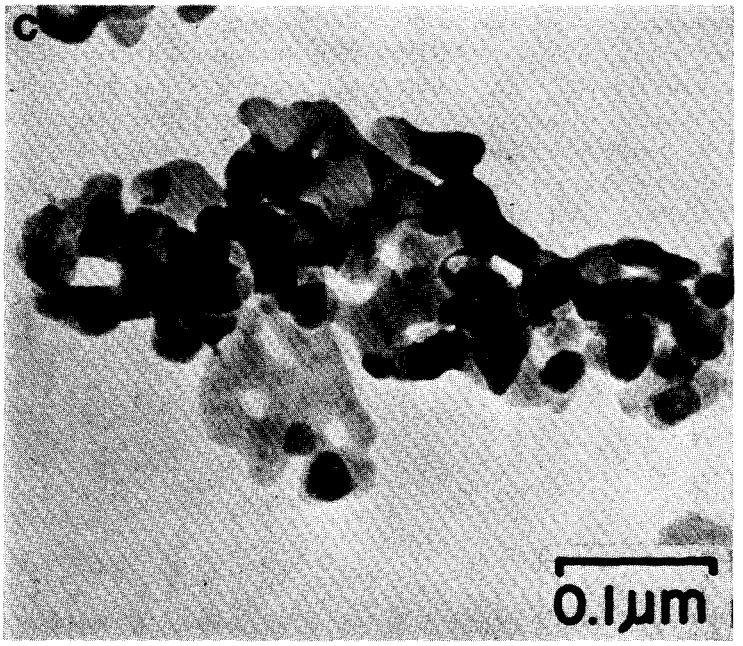

FIG. 3—*Continued.*

finely focused electron beam (the probe) which irradiates a sample area of 2 to 50 nm in diameter is scanned over the specimen. Although the beam scans the specimen, the optics are such that a stationary diffraction pattern is formed in the back focal plane of the objective lens as in TEM. The imaging lenses are used to transfer this diffraction pattern to an electron detector. The transmitted beam is intercepted by the detector, and as the probe scans the specimen the intensity variation of this beam is displayed on a synchronously scanned cathode ray tube as a bright field image. While observing the scanning image, the electron probe can be stopped and electronically positioned at any point on the specimen. With the beam stationary at a point of interest, microanalytical and microdiffraction information can be obtained.

The X-ray spectrum from a specimen induced by the electron probe can be measured by a solid state detector positioned nearby. The specimen holder is tilted towards the detector to optimize detection of the X rays. In conventional scanning electron microscopy, the area analyzed is limited to about one square micrometer because of beam spreading in the specimen. In STEM this beam spreading is minimized since the specimens are essentially transparent to the electron beam. The analyzed area in STEM is, therefore, of the size close to the area covered by the electron probe. Stray electrons and X rays in the microscope can give rise to background characteristic X rays, and to be assured that this background has been minimized, reference spectra were measured with the probe positioned in the empty areas between particles. Continuum X rays generated in the specimen can give rise to characteristic X rays from adjacent areas of the specimen. To minimize this source of spurious X rays, isolated catalysts particles were chosen for analysis. Even under these conditions, the effects of specimen generated continuum X rays may not be completely eliminated (*3*).

The X-ray data were quantified according to a method proposed by Cliff and Lorimer (*4*) as represented by the following expression:

$$I_A/I_B = k_{AB}(X_A/X_B),$$

where $I_{A,B}$ are the measured characteristic X-ray intensities and $X_{A,B}$ are the atomic fractions of elements A and B, respectively. The following reported values for the proportionality constants k_{AB} were used: $k_{CuZu} = 0.933$ and $k_{CrZn} = 1.76$. These values were experimentally determined for uniform samples of known composition at a beam energy of 80 kV. No corrections for either X-ray absorption or fluorescence were necessary for specimens thinner than 0.1 μm (*4*).

In STEM, the diffraction pattern that is formed in the back focal plane of the objective lens can be projected and photographed in the conventional manner. The area of the specimen that contributes to the diffraction pattern is determined by the probe diameter. Diffraction patterns can be obtained from areas as small as 2 nm^2 in STEM compared to the 1 μm^2 areas represented in the usual selected area diffraction patterns obtained in TEM. The microdiffraction pattern in STEM is an array of disks as compared to the points obtained in conventional selected area diffraction in TEM. This is because the electron beam is convergent upon the specimen, and the objective lens is unable to refocus the diffracted beams back to a spot as shown in Fig. 1. Each disk is actually an image of the aperture in the second condenser lens which defines the probe. Errors in determination of angles between the rows of diffraction spots and of relative lattice spacings were estimated by repeated measurements of these parameters from STEM microdiffraction patterns of well-developed crystals of known structures. For MoO_3 crystals oriented with their [100] axis perpendicular to the STEM optical axis, the measured angle between the [100] and [001] zones was found to be 89.7 $\pm$ 0.3°, compared to theoretical 88° (*5*); the ratios of measured lattice spacings were to within 1% from theoretical. For Cu metal particles, the angles between the [100] and [111] zones were found to within 1.5° and the spacings to within 2.1% of the theoretical values. Based on these measurements, the summary estimates of errors of microdiffraction in STEM is up to 2° in angles and up to 2.5% in lattice spacings, providing that no further

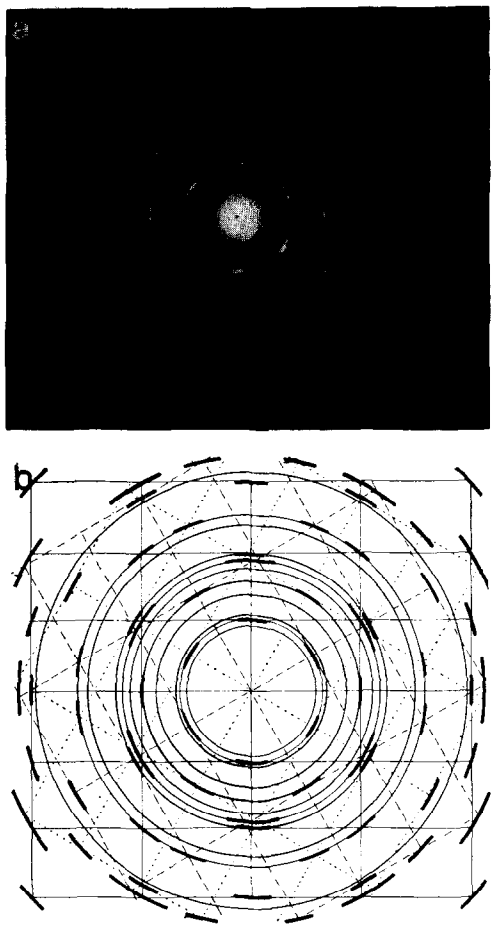

FIG. 4. (a) Selected area diffraction pattern of the star-shaped dendrite of ZnO shown in Fig. 5b. (b) Derived pattern assuming three orientations of $10\bar{1}0$ ZnO with each rotated 120° with respect to the others.

errors are compounded by photographic reproduction of the diffraction patterns.

III. RESULTS

Morphology and Crystal Structure

Pure components Cu, CuO, Cr_2O_3, and ZnO. Specimens of pure copper, copper(II) oxide, and chromia were found to be opaque to the electron beam in TEM and STEM, and therefore the morphologies of these materials were determined with scanning electron microscopy. SEM micrographs of CuO, Cu, and Cr_2O_3 are shown in Figs. 2a, 2b, and 2c, respectively. The precipitation of $Cu_2(OH)_3NO_3$ and subsequent calcina-

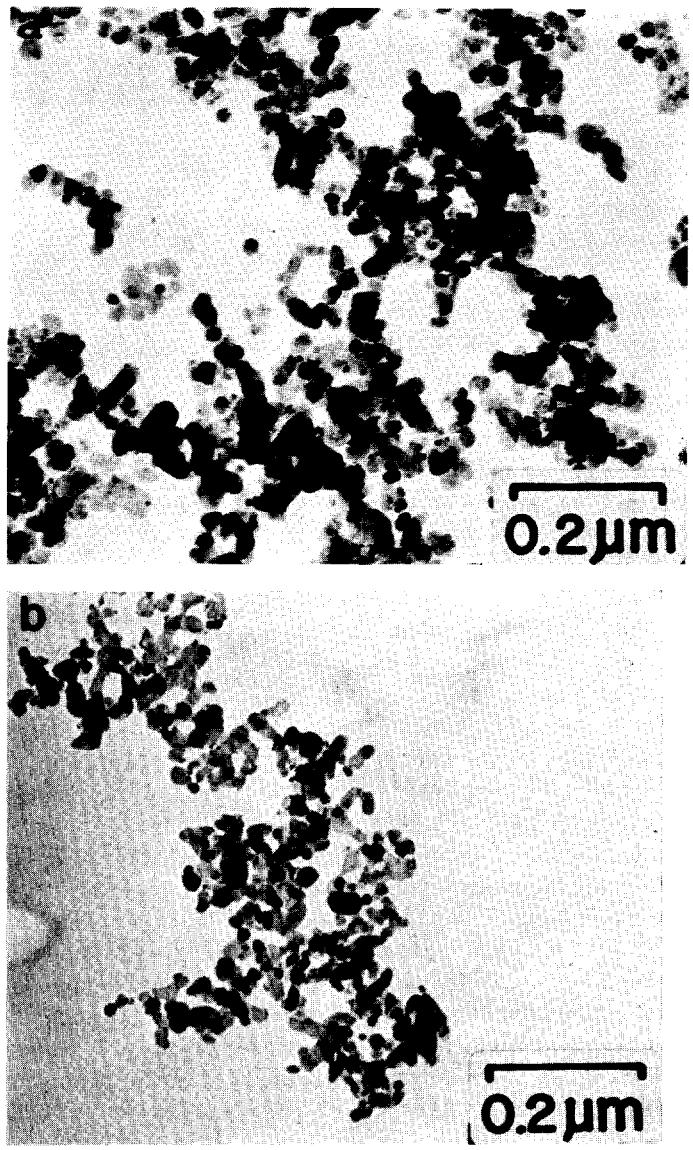

FIG. 5. Transmission electron micrographs of 10/90 CuO/ZnO specimens. (a) after calcination, (b) after reduction, and (c) after use.

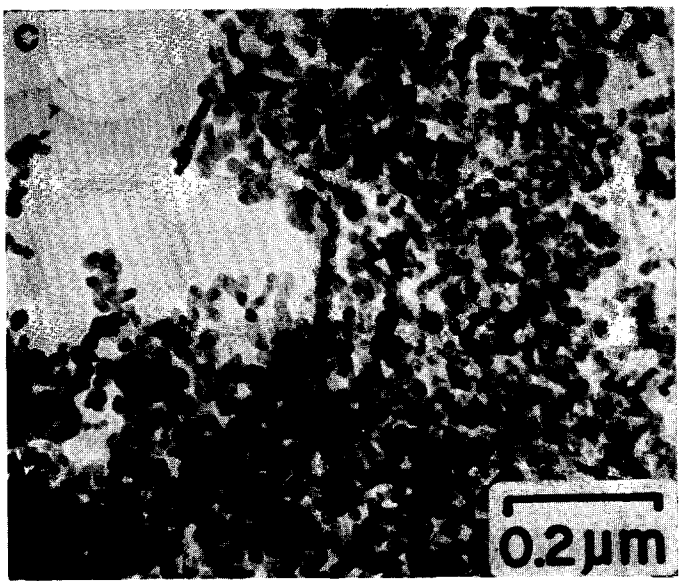

FIG. 5—*Continued.*

tion in air resulted in an interconnected network of crystallites of CuO, as shown in Fig. 2a. The morphology characteristic of CuO was needlelike or plateletlike with sharp irregular edges.

Upon reduction of the CuO specimens to copper, the original network was apparently preserved as shown in Fig. 2a. The morphologies of the copper crystallites were, however, different from the parent copper-(II) oxide. The copper crystallites had an irregular rodlike shape. The plateletlike and needlelike morphologies seen in CuO were not present in the reduced specimens. The characteristic morphology of the Cr_2O_3 crystallites was that of angularly shaped platelets which formed loose agglomerates as shown in Fig. 2c.

Pure zinc oxide crystallized with a much smaller particle size than those found for Cu, CuO, and Cr_2O_3. TEM was, therefore, better suited for characterizing the morphology of ZnO. Figs. 3a, 3b, and 3c show electron micrographs at ZnO at magnifications of 8,000, 50,000, and 180,000×, respectively. Figure 5a indicates that the precipitation of $Zn_5(OH)_6(CO_3)_2$ and its subsequent calcination resulted in ZnO dendrites, which consisted of a lacelike network of thin crystallites shown in more detail in Fig. 3b. The electron micrograph of separated zinc oxide particles at high magnification (Fig. 3c) demonstrated that the individual crystallites were thin and had major dimensions of the order of 10 to 15 nm.

Selected area electron diffraction in TEM from a ZnO dendrite shaped like a six-pointed star, shown in Fig. 3b, gave the pattern represented in Fig. 4a.[1] This diffraction pattern was found to be a superposition of diffraction patterns from six orientations of the $(10\bar{1}0)$ planes with the [0001] direction in each orientation being parallel to the plane of the star and perpendicular to the axis of each arm. Only three orientations of the $(10\bar{1}0)$ planes, parallel to the star plane, need be considered to construct the expected pattern from the star. A derived diffraction pattern is shown

[1] The starlike dendrites were found to be common in specimens of ZnO. Several of them are apparent in the low-magnification micrograph shown in Fig. 3a.

in Fig. 4b based on three orientations of $(10\bar{1}0)$, each rotated 120° relative to the others. The reciprocal lattice points in this pattern were arched to simulate a small spread in the $(10\bar{1}0)$ zone axis. The constructed pattern is in good agreement with the electron diffraction pattern obtained experimentally. It has been concluded, therefore, that the thin ZnO crystallites, such as shown in Fig. 3c, have the $(10\bar{1}0)$ planes parallel to the star plane.

Treatment of ZnO under the reduction conditions used for the catalyst preparation or testing had no apparent effect on the original oxide morphology or structure.

Binary systems CuO/ZnO and Cu/ZnO. Specimens with the following compositions in terms of CuO/ZnO mol percents were

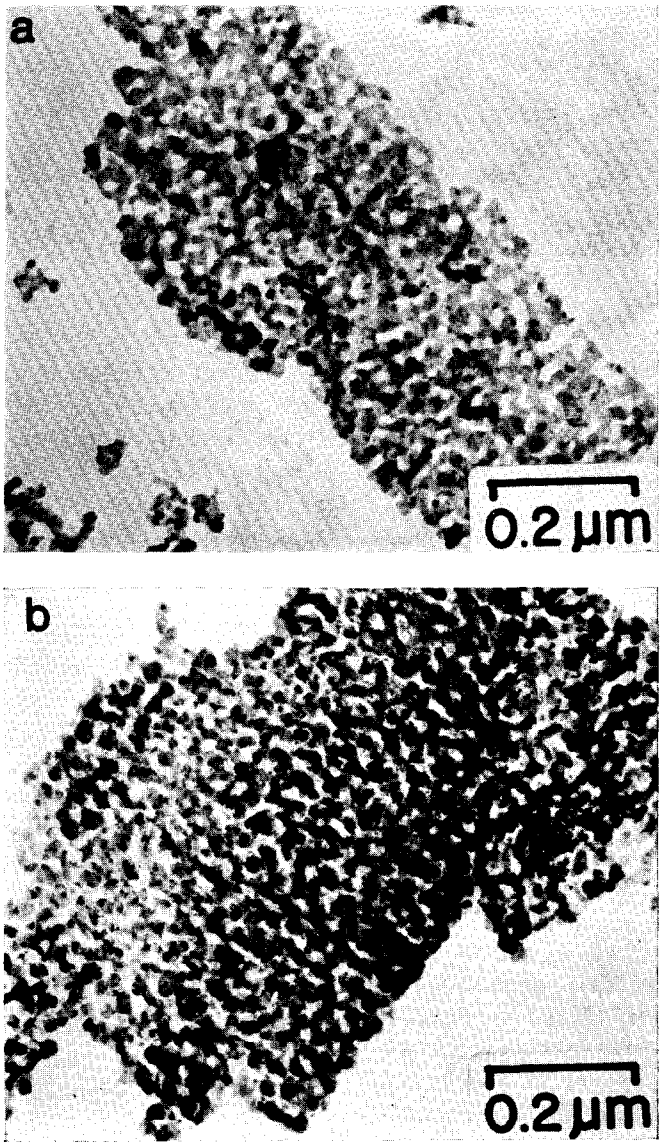

FIG. 6. Transmission electron micrographs of 30/70 CuO/ZnO specimens. (a) after calcination, (b) after reduction and (c) after use. Copper particles on the order of 8 to 10 nm can be seen on the surface of ZnO in (c).

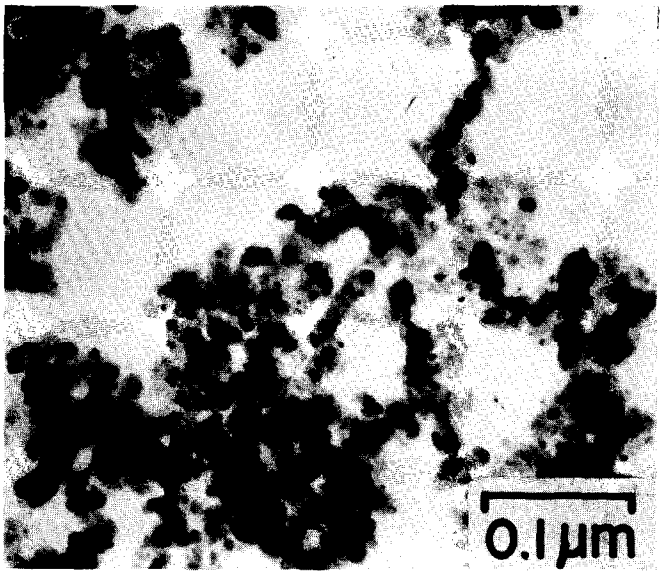

FIG. 6—*Continued.*

characterized after calcination, reduction, and testing for catalytic activity: 2/98, 5/95, 10/90, 15/85, 20/80, 30/70, 40/60, 50/50, and 67/33. A strikingly different morphology was observed for the composition range 40/60 to 67/33 compared to the morphology found in the 2/98 to 30/70 specimens. Details of the results are described separately for the 2/98 to 30/70 and 40/60 to 67/33 ranges of composition.

Transmission electron micrographs of calcined, reduced, and used specimens are shown in Figs. 5 and 6 for the 10/90 and 30/70 compositions, respectively. These micrographs, also characteristic of the 15/85 and 20/80 specimens, demonstrate that there were no major differences in the morphologies of the different compositions within this range. The ZnO phase has a morphology consisting of an interconnected network of thin crystallites similar to that of pure ZnO. No CuO or Cu particles were found in the 2/98 catalysts but for compositions between 5/85 and 30/70, the CuO phase in the calcined specimens and the Cu phase in both the reduced and used specimens were seen in the electron micrographs as circular (or spherical) particles approximately 5–8 nm in diameter on the

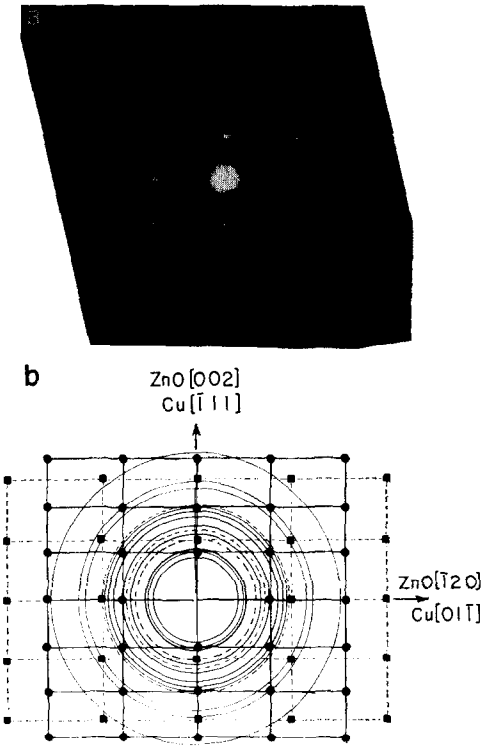

FIG. 7. (a) Selected area diffraction pattern from reduced 30/70 specimen. (b) Schematic diffraction pattern showing the spots from ZnO (●) and Cu (■). The circles with the solid lines and the circles with dashed lines are the more intense diffraction rings from ZnO and Cu, respectively.

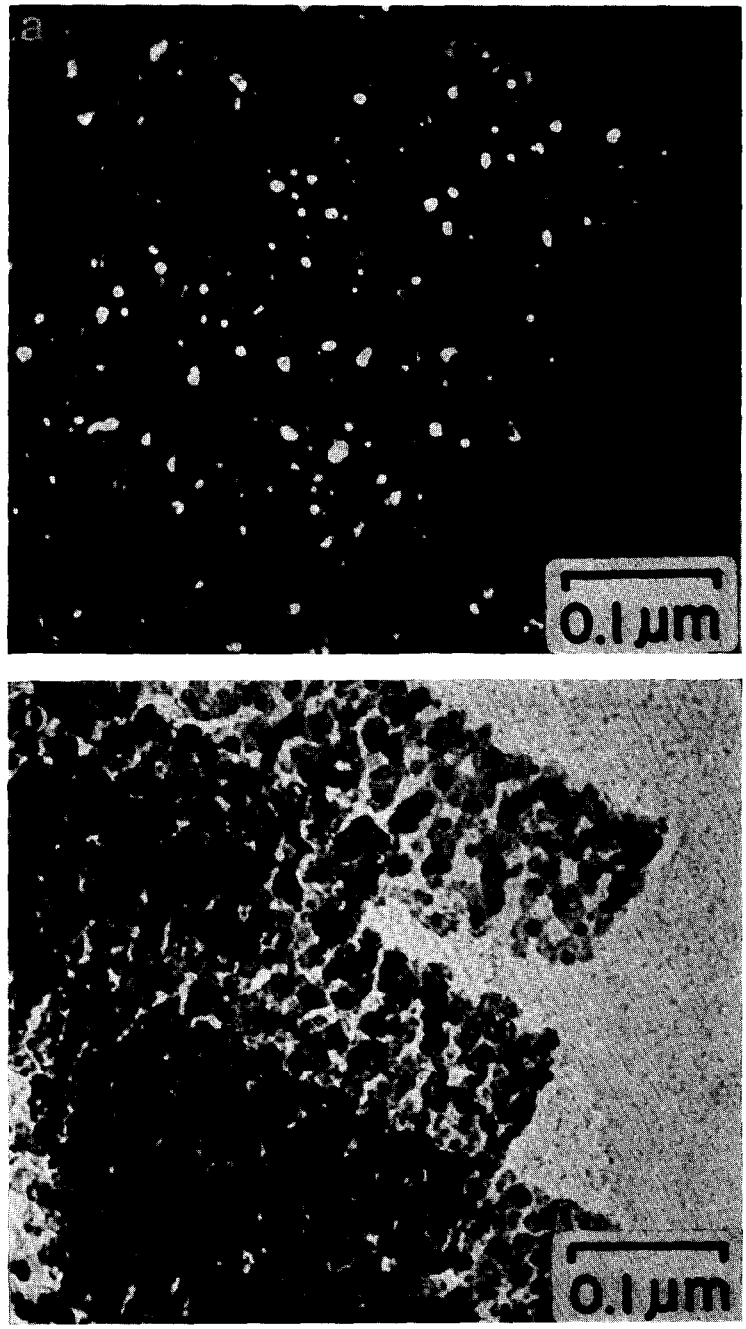

FIG. 8. (a) Dark field transmission electron micrograph of 30/70 reduced specimen. (b) Bright field micrograph of same area.

surface of the ZnO. The density of the CuO and Cu particles increased as the relative concentration of copper in the mixture increased.

Selected area electron diffraction patterns were taken for the 30/70 calcined and the 30/70 reduced specimens. The diffraction pattern for the *calcined* specimen

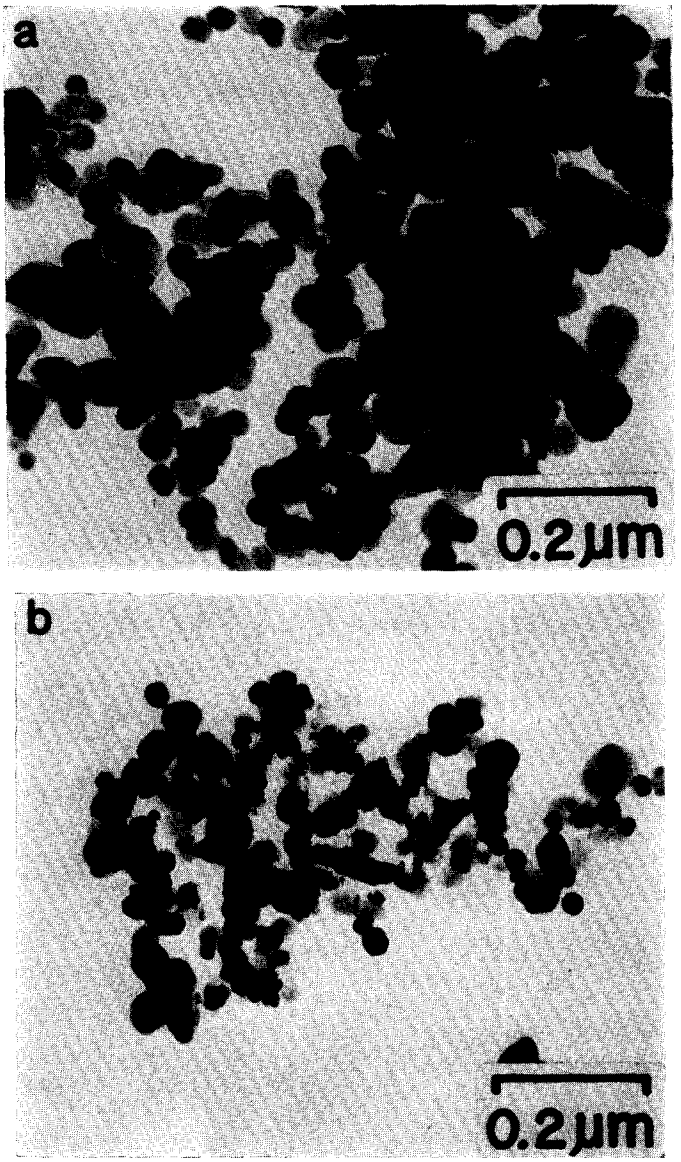

FIG. 9. Transmission electron micrographs of 40/60 CuO/ZnO specimens. (a) after calcination and (b) after reduction. Note the presence of angular-shaped particles.

showed spots from a $(10\bar{1}0)$ orientation of zinc oxide in addition to rings from cupric oxide. A significant fraction of the zinc oxide crystallites had their $(10\bar{1}0)$ planes aligned parallel to their surfaces as was found for pure ZnO. The diffraction pattern of the 30/70 *reduced* specimen also showed the same spot pattern of zinc oxide as the calcined sample, but in addition to rings from Cu, a spot pattern of copper was also observed, Fig. 7. A significant fraction of the copper particles exhibited an epitaxial relationship with the ZnO substrate such that the Cu (211) plane was parallel to ZnO $(10\bar{1}0)$ and the Cu $[\bar{1}11]$ axis parallel to ZnO [0001] axis. The copper $(\bar{1}11)$ diffraction spot was used to obtain a dark field electron micrograph of the oriented

copper crystallites in the reduced 30/70 specimen. Fig. 8a shows the resulting dark field image and Fig. 8b shows the corresponding bright field image of the same area. The dark field image was also obtained from a copper [$\bar{1}11$] diffraction spot located on the Cu (111) ring in a direction *not aligned* with the ZnO [0001] axis. An estimate of the relative numbers of copper particles aligned and nonaligned with ZnO [0001] was made based on the assumption that the nonaligned particles were randomly oriented. The particles in dark field images through aligned and nonaligned Cu [$\bar{1}11$] spots were counted with the result that 70 $\pm$ 10% of Cu particles were oriented with their (211) plane parallel to the ($\bar{1}$010) plane of the zinc oxide.

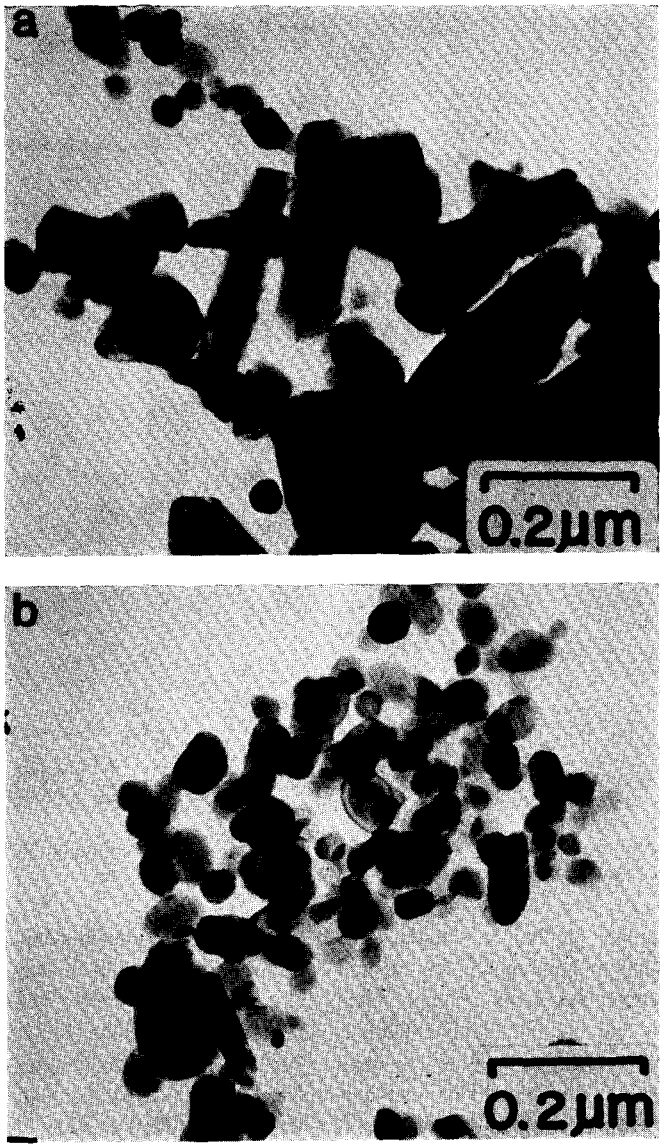

FIG. 10. Transmission electron micrographs of 50/50 CuO/ZnO specimens. (a) and (b) after calcination and (c) after reduction.

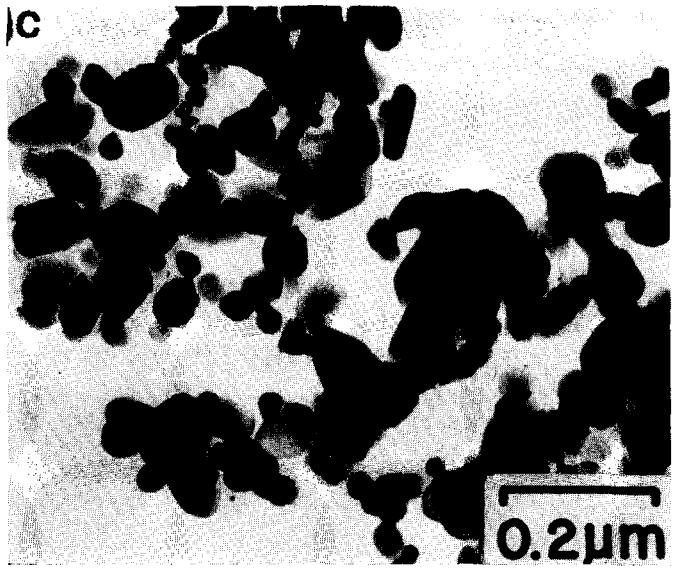

FIG. 10—*Continued.*

Transmission electron micrographs of calcined, reduced, and used specimens of compositions 40/60, 50/50, and 67/33 were observed and are shown in Figs. 9, 10, and 11, respectively. The interconnected network of ZnO crystallites characteristic of the 2/98 to 30/70 specimens was not present in the 40/60 to 67/33 specimens. In comparison with the 2/98 to 30/70 specimens, the particles of the components in the 40/60 to 67/33 range were larger. Microanalysis and microdiffraction in STEM were used to identify the morphology and crystal structure associated with each of the components. The larger particles and the needles seen in the calcined specimens were CuO. The morphologies of CuO in these specimens were similar to the morphologies observed in pure CuO as shown in Fig. 2b. During reduction and use, the original CuO particles in the 40/60 to 67/33 specimens changed their shape to that of irregular crystallites of copper metal. This change in morphology was found to be comparable to that observed upon the reduction of pure CuO to Cu. In addition, some preferential orientation of copper was revealed by STEM microdiffraction which indicated a frequent orientation of the Cu (110) planes parallel to the surface of the supporting film.

The ZnO particles in the 40/60 to 67/33 specimens were separate crystals of platelet appearance with major dimensions of the order of 70 to 120 nm, frequently with hexagonal plan outline (Figs. 9–11). No significant differences in the morphology of these particles were found for the calcined, reduced, and used specimens. Microdiffraction in STEM with a spot size of 23 nm focused on a small area within the platelet resulted in a pattern shown in Fig. 12. Inspection of this pattern showed that it had nearly, but not precisely, hexagonal symmetry which would be expected if the ZnO (0001) basal planes were the platelet major surface planes. The deviations from perfect hexagonal symmetry amounted to up to 3° in the angle between rows of spots and up to 2.5% in the ratio of spacings between spots in different directions. These deviations were barely outside the limits of error of microdiffraction in STEM (cf. experimental section) but could be caused by a real

distortion of the ZnO crystallites due to the presence of other components in the system.

Ternary systems $CuO/ZnO/Cr_2O_3$ and $Cu/ZnO/Cr_2O_3$. The 60/30/10 CuO/ZnO/Cr_2O_3 and Cu/ZnO/Cr_2O_3 specimens displayed all of the morphologic features observed in the 67/33 CuO/ZnO and Cu/ZnO specimens, and in addition crystals of Cr_2O_3 were found among the other components. Transmission electron micrographs were taken of the ternary system after calcination and after use. The Cr_2O_3 crystallites were the largest particles in these specimens. Some of the Cr_2O_3 crystallites had a hexagonal shape, and selected area electron diffraction from these crystallites gave a hexagonal pattern of the (0001)

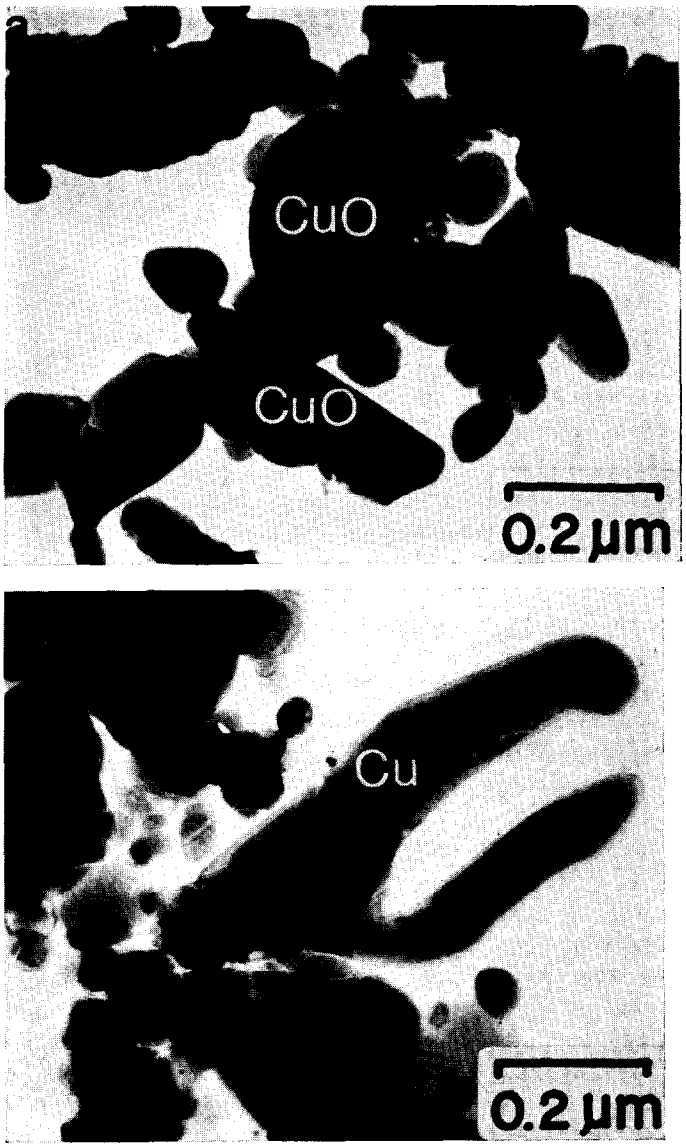

FIG. 11. Transmission electron micrographs of 67/33 CuO/ZnO specimens. (a) after calcination, and (b) and (c) after reduction. Note the presence of angular-shaped particles.

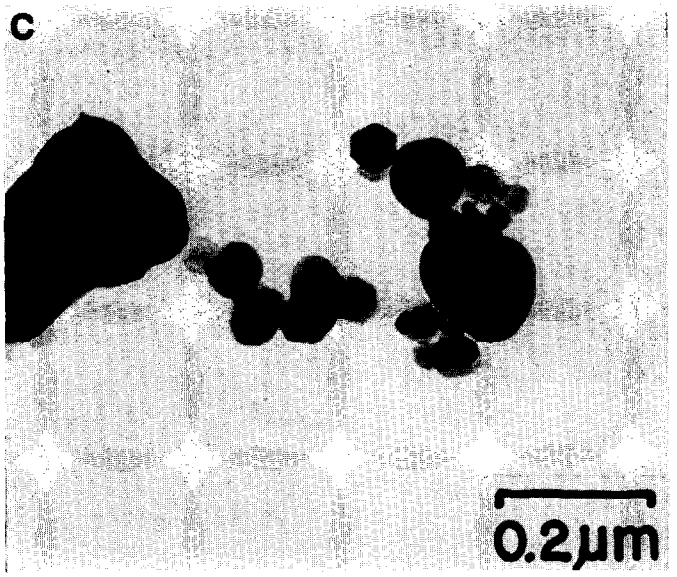

FIG. 11—*Continued.*

orientation of the corundum structure of Cr_2O_3. The CuO needlelike crystallites were present in the calcined specimens and changed upon reduction to the copper morphology in a manner similar to that observed in the 67/33 binary system. The particles displayed the similar morphologies as found in 67/33 specimens, and the small hexagonal platelets were identified as ZnO.

Compositional Analysis

Compositional analysis of the catalysts in STEM were directed primarily at determining the extent of dissolved copper in the zinc oxide phase. A nominal probe size of 5.8 nm was used in analyzing the reduced 10/90, 20/80, and 30/70 catalysts. The results were represented as distributions of copper content as shown in Fig. 13. The probe was positioned on the specimen at random and the observed distribution profiles resulted from the varying overlap of the probe with particles containing copper. To obtain information on mutual solubility of catalyst components, the measured distribution curves were compared with those calculated from models based on the measured particle sizes and average distances. Two model distribution curves were constructed for the 30/70 catalyst, assuming that the copper signal was proportional to the overlap area between the probe and circular, 8-nm diameter, copper particles spaced by their experimentally determined average distance of 19 nm. The probe position was selected by a two-dimensional random number generator. To correct for scattered electrons within the specimen, the probe diameter was assumed larger than the nominal diameter, i.e., 8 and 15 nm for the two model distributions.[2] These distributions are plotted in Fig. 14, and the shaded area between them comprises the expected

[2] The total electron beam spreading in the 30/70 catalyst was estimated from formula (13) in Ref. (3). Taking the thicknesses of the ZnO platelets and of the carbon film to be 15 and 40 nm, respectively, the cumulative spreading was calculated to be 2 nm, which would broaden the 5.8 nm probe diameter to 7.8 nm. With copper particles present, 8-nm thick crystallites would cause an additional broadening of 0.7 nm. The probe sizes of 8 to 15 nm assumed in the two model calculations thus provide a sufficient error margin for the estimated probe spread.

FIG. 12. Microdiffraction from a hexagonal ZnO particle in the 67/33 specimen.

results of copper microanalysis for probe diameters between 8 and 15 nm. The actual copper concentrations, represented by experimental points and corresponding error bars in Fig. 14, were found to be significantly higher than those obtained from models assuming copper-free zinc oxide mixed with 8-nm copper particles. This result thus provides evidence for a subresolution dispersion, including possible solution, of copper in the zinc oxide.

For specimens in the composition range 40/60 to 67/33 analyses of separated, and in some cases completely isolated particles, were possible. The results for the reduced specimens 40/60, 50/50, and 67/33 are shown in Fig. 15. Since the diameters of the individual particles were 70 nm and larger, a probe size of 23 nm was used. Average copper concentrations of 5.0 ± 3.7, 8.7 ± 3.6, and 11.6 ± 2.8% were found in the ZnO particles in the 40/60, 50/50, and 67/33 specimens, respectively. Assuming that the effects of specimen-generated continuum X rays was minimal, these results suggest that copper is indeed soluble in the zinc oxide, under reducing conditions, up to approximately 11 to 12%.

The solubility of copper in zinc oxide was found to be less for specimens that had been only calcined. The average copper concentrations in ZnO for calcined specimens 50/50 and 67/33 were 6.1 ± 2.4 and 6.4 ± 2.4%, respectively. The distribution of copper concentration for each of these specimens is shown in Fig. 16. Qualitative analyses of the used $Cu/ZnO/Cr_2O_3$ catalysts also indicated solubility of copper in zinc oxide. In addition, chromium was found to be present in the zinc oxide phase along with the copper and to increase the amount of dissolved copper up to 16%.

IV. DISCUSSION

Catalyst morphology. The two distinct zinc oxide morphologies, namely, the interconnected network of thin crystallites at copper concentrations 0–30% and the hexagonal platelets at higher copper concentrations, appear to be determined by the crystal structure of the catalyst precursors in the precipitates. The fact that the morphology of zinc oxide is comparable in each of the specimens over the composition range 0 to 30% copper indicates that the zinc oxide morphology is determined by the $Zn_5(OH)_6(CO_3)_2$ precursor precipitate. The presence of $(Cu,Zn)_2(OH)_2$

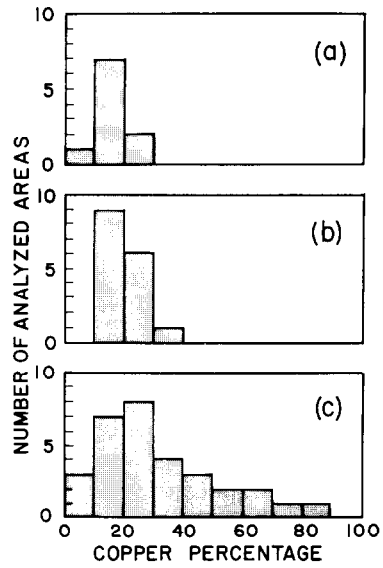

FIG. 13. Histograms of the copper concentration from areas analyzed at random for reduced specimens (a) 10/90, (b) 20/80, and (c) 30/70. Beam diameter 5.8 nm.

CO_3 has little influence on the zinc oxide morphology in the 0 to 30% catalysts. The appearance of the hexagonal platelet morphology and increase in particle size of zinc oxide at 40% Cu coincides with the appearance of a significant amount of $Cu_2(OH)_3NO_3$ in the precipitate. Apparently this platelet growth is induced by the presence of $Cu_2(OH)_3NO_3$ in the calcination stage at which ZnO begins to nucleate by the decomposition of the carbonates $Zn_5(OH)_6(CO_3)_2$ and $(Cu,Zn)_2(OH)_2CO_3$. The higher decomposition temperature of $Cu_2(OH)_3NO_3$ may be the key factor in producing the changes in oxide morphology. It is suggested that zinc oxide nucleates and grows on the surface of the relatively stable $Cu_2(OH)_3NO_3$ before this compound itself begins to decompose. This nucleation mechanism is supported by a good structural match between the basal ZnO (0001) plane and the pseudohexagonal (001) plane

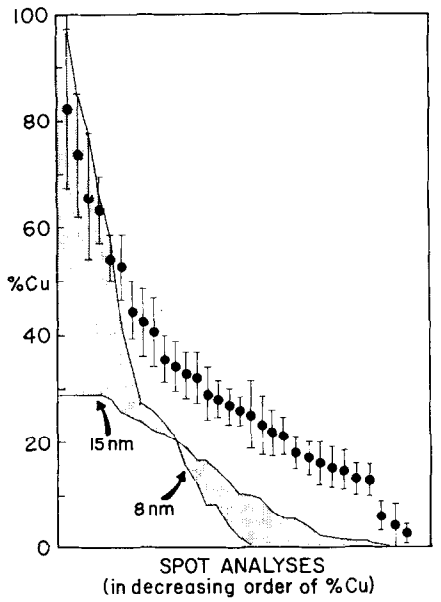

FIG. 14. Copper compositions of 30/70 reduced specimen plotted (solid circles) in order of decreasing copper concentration for a beam diameter of 5.8 nm. Shaded area represents copper concentration from simulated analysis for beam diameters between 8 and 15 nm.

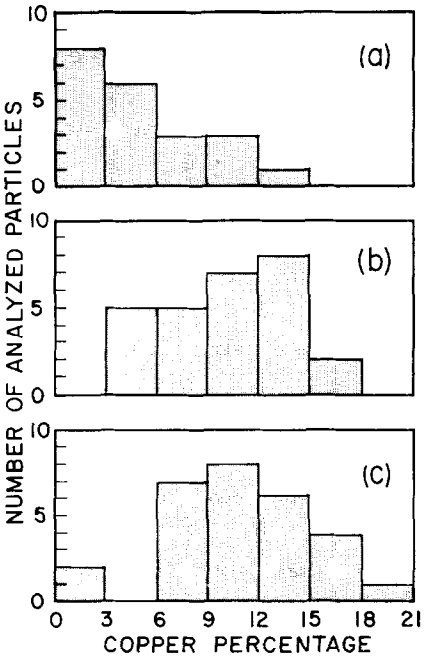

FIG. 15. Histogram of the copper concentration in ZnO particles of reduced specimens (a) 40/60, (b) 50/50, and (c) 67/33. Beam diameter 23 nm.

of $Cu_2(OH)_3NO_3$ (*1*), and explains the otherwise uncommon basal growth of ZnO. After the completion of calcination and reduction, the copper compound segregates as metallic copper but the ZnO crystallites do not undergo further morphologic changes.

The CuO dispersion produced as the final result of calcination and the dispersion of the subsequently reduced copper may be determined by the decomposition of the precursor precipitates $(Cu,Zn)_2(OH)_2CO_3$ and $Cu_2(OH)_3NO_3$. The carbonate $(Cu,Zn)_2(OH)_2CO_3$ is the predominant copper containing precipitate in the 2 to 30% specimens, both $(Cu,Zn)_2(OH)_2CO_2$ and $Cu_2(OH)_3NO_3$ are present in the precipitate for the 40% preparation, and $Cu_2(OH)_3NO_3$ predominates for copper concentrations above 40%. $(Cu,Zn)_2(OH)_3CO_3$, which decomposes at relatively low temperatures and contains intimately mixed copper and zinc, apparently gives rise to the fine dis-

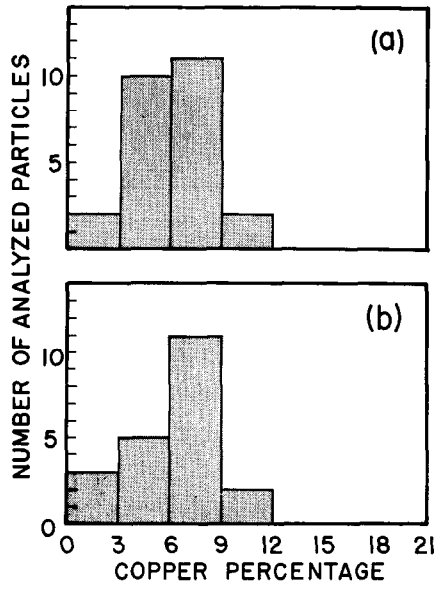

FIG. 16. Histogram of the copper concentration in ZnO particles of calcined specimens (a) 50/50 and (b) 67/33. Beam diameter 23 nm.

persions while $Cu_2(OH)_3NO_3$, which decomposes at a higher temperature, closer to the final calcination temperature of 350°C, gives rise to the larger crystals of CuO. Consequently, after reduction of the oxides, fine dispersions of metallic copper exist in the 10 to 30% copper catalysts while relatively large crystals of copper occur in the 40 to 67% copper catalysts. The similarities of the morphologies found for pure copper oxide and pure copper with the copper oxide and copper in the 40 to 67% copper catalysts support this interpretation.

The addition of chromia after the precipitation step in the preparation of the ternary catalyst had no apparent effect on the catalyst morphology and structure. The similarities of the morphologies of the copper, copper oxide, and zinc oxide components with that found for the 67/33 catalyst suggest that the mechanisms for the formation of the 60/30/10 Cu/ZnO/Cr_2O_3 and the 67/33 Cu/ZnO catalysts are the same.

Composition and structure of catalyst particles. The binary catalysts with 5 to 30% copper contain crystalline, near spherical, copper particles of fairly uniform size 7 to 8 nm, oriented with their (211) face toward the underlying ($\bar{1}010$) ZnO surface. Such a composite comprises rather well-defined metal–semiconductor contact areas through which electron exchange may take place between the copper and zinc oxide phases. Indeed, the optical *d*-hump transition of copper in the 30/70 catalyst is shifted to energies lower than those in pure copper metal (*1*) which suggests that electron transfer occurs from the copper particles into the zinc oxide phase. From a chemical point of view, the observed shift of electron density will leave the copper particles in an effectively oxidized state and the zinc oxide in a reduced state compared to their respective pure phases. The observed *d*-hump shift is small, however, and only a small fraction of electrons, estimated at 0.05 electron per Cu atom, is transferred from one phase into the other.

An additional and more profound chemical interaction in the 2/98 to 30/70 catalysts is suggested by the results of STEM microanalyses which indicated the presence of subresolution copper species in the zinc oxide. It is this second form of copper which is believed responsible for the black color and an extensive near-infrared absorption of the Cu/ZnO catalysts, interpreted in Part I as transitions between the filled levels of Cu(I) ions dissolved in ZnO and the conduction band of the latter. The 30/70 Cu/ZnO catalyst is thus characterized as a complex but well-defined system containing two forms of copper, one appearing in and strongly interacting with the zinc oxide phase and the other being a fine copper metal dispersion acting as a weak electron donor to the zinc oxide phase across the Cu(211)/ZnO($10\bar{1}0$) interface.

For concentrations of 40% copper and above, the ZnO particles in the binary catalysts were shown by X-ray micro-

analysis to contain approximately 6% copper after calcination and up to above 12% copper after subsequent reduction, without the appearance of a crystal structure other than hexagonal ZnO. During calcination, therefore, Cu(II) reaches a solubility limit of 6% which is within the range of previously published values (*6*, *7*). During reduction, the copper segregates as a separate, metallic phase and is also dissolved in ZnO. The metal particles are large and their *d*-hump energies coincide with those of pure copper (*1*). The contact between the copper particles and the ZnO crystallites is loose and the basal (0001) ZnO faces, as well as some edge surfaces, are exposed. Based on these observations, the electron exchange through a Cu/ZnO interface appears to be less significant with the copper-rich, 40% copper and above, catalysts than with the 5/95 to 30/70 catalysts. However, the optical absorption due to copper dissolved in ZnO persists even in the copper-rich catalysts (*1*). Copper most likely exists in ZnO as Cu(I), because this ion is isoelectronic with Zn(II) and assumes most frequently tetrahedral coordination. The dissolution of Cu(I) in ZnO may occur by one or more of the following reactions, where the defect notation usage is that of Kofstad (*8*).

$$Cu_2O \rightarrow Cu'_{Zn} + Cu_i^{\cdot} + O_0 \quad (1)$$

$$Cu_2O \rightarrow 2Cu'_{Zn} + V_0^{\cdot\cdot} + O_0 \quad (2)$$

$$Cu_2O \rightarrow 2Cu'_{Zn} + Zn_i^{\cdot\cdot} + O_0 \quad (3)$$

The solubility of the Cu(I) ions may be limited by the concentration of Cu(I) interstitials (reaction (1)), oxygen vacancies (reaction (2)), or zinc interstitials (reaction (3)) that the ZnO lattice can accommodate.

In each of the reactions (1)–(3), the Cu(I) solubility may be increased by the presence of trivalent ions such as Cr(III) which compensate for the charge deficiency of the Cu(I) centers according to Eq. (4).

$$Cu_2O + Cr_2O_3 \rightarrow 2Cu'_{Zn} + 2Cr''_{Zn} + 4O_0 \quad (4)$$

This model is indeed consistent with the analyses of the $Cu/ZnO/Cr_2O_3$ catalyst which show an increase of copper content in ZnO due to the presence of Cr(III) above that of the copper content in the chromia-free Cu/ZnO catalysts. Thus, these analyses lend further support to the proposition forwarded on the basis of electronic spectra (*1*) that a solid solution of Cu(I) in ZnO is formed in the reduced catalysts.

Relation to catalyst activity. Results of catalyst testing reported in Part I showed that the Cu/ZnO catalysts, especially the 30/70 Cu/ZnO and 67/33 Cu/ZnO, had a substantial activity in methanol synthesis at 75 atm and 250–300°C. Since copper in the Cu/ZnO catalysts with copper concentrations higher than 40% had the same morphology and low surface area as the copper metal that was found to be inactive, the activity of the 67/33 Cu/ZnO catalyst cannot be attributed to copper metal. The highly dispersed copper metal in the Cu/ZnO catalysts with copper concentrations of 30% and below, however, is in good contact with the ZnO, has a slightly reduced *sp*-electron density, and may have chemisorption properties to reacting gases that differ from those of the larger and separated copper metal particles.

In either case, the presence of zinc oxide appears essential for catalytic activity, and the catalysts containing both the ZnO $(10\bar{1}0)$ orientation in the 2/98 to 30/70 compositions and the well-developed hexagonal platelets with (0001) orientation in the 40/60 to 67/33 catalysts are active and selective for low pressure methanol synthesis. Similarly, the Cr_2O_3 containing catalyst containing hexagonal platelet ZnO crystallites was an active synthesis catalyst (*1*). A feature common to ZnO in both the Cu/ZnO and $Cu/ZnO/Cr_2O_3$ systems is

the high content of copper dissolved in ZnO. This is a major difference from the chemical properties of the pure components and is considered the most important cause of the promotion effects in the Cu/ZnO system. The electron transfer between copper metal and ZnO in the 30/70 catalyst may play a contributory but not an essential role in the synthesis since good catalysts exist in which the Cu/ZnO contact is not well established.

ACKNOWLEDGMENTS

The authors thank the Pennsylvania Science and Engineering Foundation and the National Science Foundation for their support of these studies.

REFERENCES

1. R. G. Herman, K. Klier, G. W. Simmons, B. P. Finn, J. B. Bulko, and T. P. Kobylinski, *J. Catal.* **56**, 407 (1979).
2. K. Klier, R. G. Herman, and T. P. Kobylinski, *in* "9th Central Regional Amer. Chem. Soc. Meeting, Charleston, W. A., October 1977," Abstr. No. INOR-53; R. G. Herman, K. Klier, and B. P. Finn, *in* "12th Middle Atlantic Regional Amer. Chem. Soc. Meeting, Hunt Valley, Md., April 1978," Abstr. No. PH-43.
3. J. S. Goldstein, J. L. Costley, G. W. Lorimer, and S. J. B. Reed, *in* "Proceedings, 10th SEM IITRT, 1977," Part I, p. 315.
4. G. Cliff and G. W. Lorimer, *in* "Proceedings, 5th Europ. Congr. EM, Institute of Physics, London, 1972," pp. 140–141.
5. G. Thomas, "Transmission Electron Microscopy of Metals," p. 117. Wiley, New York, 1966.
6. F. H. Chapple and F. S. Stone, *Proc. Brit. Ceram. Soc.*, **1**, 45 (1964).
7. M. Schiavello, F. Pepe, and S. DeRossi, *J. Phys. Chem.* **92**, 109 (1974).
8. P. Kofstad, "High Temperature Oxidation of Metals," pp. 51–87. Wiley, New York, 1966.